BBA - Bioenergetics 1866 (2025) 149518

Contents lists available at ScienceDirect

BBA - Bioenergetics

journal homepage: www.elsevier.com/locate/bbabio

# Finding the *E*-channel proton loading sites by calculating the ensemble of protonation microstates

Md. Raihan Uddin [a,c], Umesh Khaniya [b,g], Chitrak Gupta [d,e], Junjun Mao [a], Gehan A. Ranepura [a,g], Rongmei Judy Wei [a,f], Jose Ortiz-Soto [a,f], Abhishek Singharoy [d,e], M.R. Gunner [a,c,*]

[a] Department of Physics, The City College of New York, NY 10031, USA
[b] National Cancer Institute, NIH, Bethesda, MD 20814, USA
[c] Graduate Program In Biochemistry, The Graduate Center of CUNY, 365 5th Avenue, NY 10031, USA
[d] School of Molecular Sciences, Arizona State University, Tempe, AZ, USA
[e] Bio-design Institute, Arizona State University, Tempe, AZ, USA
[f] Ph.D. Program in Chemistry, The Graduate Center, City University of New York, New York 10016, USA
[g] Ph.D. Program in Physics, The Graduate Center, City University of New York, New York 10016, USA

ARTICLE INFO

*Keywords:*
Complex I
Proton transfer
Proton pump
MCCE
Microstates

ABSTRACT

The aerobic electron transfer chain builds a proton gradient by proton coupled electron transfer reactions through a series of proteins. Complex I is the first enzyme in the sequence. Here transfer of two electrons from NADH to quinone yields four protons pumped from the membrane N- (negative, higher pH) side to the P- (positive, lower pH) side. Protons move through three linear antiporter paths, with a few amino acids and waters providing the route; and through the *E*-channel, a complex of competing paths, with clusters of interconnected protonatable residues.

Proton loading sites (PLS) transiently bind protons as they are transported from N- to P-compartments. PLS can be individual residues or extended clusters of residues. The program MCCE uses Monte Carlos sampling to analyze the *E*-channel proton binding in equilibrium with individual Molecular Dynamics snapshots from trajectories of *Thermus thermuphillus* Complex I in the apo, quinone and quinol bound states. At pH 7, the five *E*-channel subunits (Nqo4, Nqo7, Nqo8, Nqo10, and Nqo11) take >25,000 protonation microstates, each with different residues protonated. The microstate explosion is tamed by analyzing interconnected clusters of residues along the proton transfer paths. A proton is bound and released from a cluster of five coupled residues on the protein N-side and to six coupled residues in the protein center. Loaded microstates bind protons to sites closer to the P-side in the forward pumping direction. MCCE microstate analysis identifies strongly coupled proton binding amongst individual residues in the two PLS clusters.

## 1. Introduction

The enzymes of the aerobic bacterial and mitochondrial electron transfer chains are multi-subunit protein assemblies, denoted as Complexes I–IV. Complex I, the first and largest enzyme, connects the soluble Krebs cycle reactions to those of the transmembrane electron transfer chain. It extends ~200 Å within the membrane with an ~150Å periplasmic arm. Proton pumps, such as Complex I, store energy via chemiosmotic coupling [1]. Protons are moved to the lower pH, more positive (P-side) compartment driven by redox reactions, moving electrons downhill to sites at more positive potential. The proton pumps establish an electrochemical proton motive force of 100 to 200 mV across the membrane [1], which in turn drives the $F_1F_0$-ATP synthase [2,3]. In mitochondria, Complex I contribute approximately 40% of the protons that build the gradient [1–5].

The energy released during the transfer of two-electrons from NADH to ubiquinone in the periplasmic domain is coupled to the translocation of four protons across the membrane domains [6]. The overall reaction is:

$$NADH + H^+ + Q \rightarrow NAD^+ + QH_2 \quad (1a)$$

* Corresponding author at: Department of Physics, City College of New York, 160 Convent Avenue, New York, NY 10031, USA.
*E-mail address:* mgunner@ccny.cuny.edu (M.R. Gunner).

https://doi.org/10.1016/j.bbabio.2024.149518
Received 10 August 2024; Received in revised form 24 September 2024; Accepted 14 October 2024
Available online 21 October 2024

$$4H^{+}_{N} \rightarrow 4H^{+}_{P} \quad (1b)$$

There are four proposed proton transfer paths: the *E*-channel, which is closest to the peripheral subunit where electron transfer takes place and three homologous antiporter domains [6]. It has been proposed that each antiporter subunit transports one proton [7,8] with the fourth proton traveling through the *E*-channel [8–10], though the number and identity of pumping pathways is by no means settled [6,9,11,12].

Protons move through membrane embedded proton pumps such as Complex I [13], bacteriorhodopsin [14], and Cytochrome c Oxidase (CcO) [15,16]. Conceptually, three elements are needed to drive protons uphill from the membrane N- to P-side [13,16]: paths, proton loading sites (PLS), and gates. Hydrogen-bonded paths permit proton transfer via the Grotthuss Mechanism [17,18]. The three antiporter paths use a few amino acids and water molecules to create a linear route for protons. In contrast, a tangle of competing paths are seen to create the *E*-channel. The E-channel pathways have been modeled using Molecular Dynamics (MD) simulations [7,19,20], and by MCCE (MultiConformation Continuum Electrostatics) Monte Carlo (MC) sampling [10].

As protons traverse proton pumps, they are temporarily held by a proton loading site (PLS). PLS residues lie along the proton transfer path and can be a single amino acid [21] or clusters of residues [10]. During the reaction sequence the PLS proton affinity rises to bind a proton and then is reduced to release it [18,21,22]. For example, in CcO changes in hydrogen bonding patterns [21,23] or water loading to an internal cavity [24] change the PLS proton affinity by over five kcal/mol. The electrochemical gradient across the membrane encourages energy dissipating proton transfer, from the P- to the N-side. Therefore, during proton loading, the PLS must connect to the N-side and to the P-side during proton release, with gates blocking proton transfers in the wrong direction.

Crystal structures and cryo-EM structures [9,12,25–35] of Complex I have laid the foundation for in-depth investigation into proton pumping paths and the energy conserving pumping mechanism. Specific buried acidic and basic residues (Asp, Glu, His and Lys) have been identified as possible PLS, as members of proton transfer paths or as helping to stabilize internal hydration [6,7,20]. The importance of many of these residues has been confirmed by site-directed mutations [36–38].

Multiple computational methods have been applied to find the proton transfer paths and the PLS, and to determine what triggers the protons to bind and release. Simulations have often focused on the linear antiporter channels [19,39–42]. MD simulations [19,41–43] have been instrumental in delineating hydrogen-bonded paths, often using trajectories with different fixed residue protonation states and cofactor redox states. Quantum Mechanics/Molecular Mechanics (QM/MM) methods have further probed local proton transfer events [19,41,42]. MD simulations involving the membrane domain of *E. coli* Complex I show that changes in protonation states of key residues can impact the hydration of channels supporting proton transfer [19,43]. Generally, the calculated paths through the antiporter subunits align with those predicted given the location of charged and polar residues in the experimental structures [41,42].

The antiporter subunits are related to the Mrp $Na^{+}/H^{+}$-antiporters [44] and the redox active periplasmic subunit is related to soluble hydrogenases [45–47] (Fig. 1). However, the *E*-channel is unique to Complex I. It is made up of five subunits, including Nqo4, with the quinone binding site in the periplasmic arm, and the integral membrane subunits Nqo7, 8, 10 and 11 (Fig. 1b) [10]. (*T. thermophilus* naming used here. See Table SI.1 for naming conventions for Complex I from other organisms.)

PLS are defined here as being residues that lie along the proton transfer path and are in different protonation states in different reaction intermediates. Thus, to identify them via computation, we need structures in different reaction states and a procedure to find the high probability protonation states. In Complex I quinone binding, reduction and release are assumed to trigger proton pumping [13,38,47–50], so apo, quinone- and quinol-bound states have been trapped experimentally [6,51,52] and modeled with MD [19,51,53,54]. The connectivity of proton transfer paths has been evaluated in Complex I structures prepared in different states [51,53]. However, MD and QM/MM must be carried out with fixed protonation states. Thus, those simulations needed to make educated guesses as to which residues bind protons, and these choices can not change during the simulation.

The MCCE program has been used to trace proton transfer paths in different proteins [10,21,22,55,56]. The program uses MC sampling to find the Boltzmann distribution of side chain position and protonation states given a fixed protein backbone [57]. MCCE finds the hydrogen bonds and protonation states that are at equilibrium with the backbone of the input structure. This stochastic method allows us to characterize paths through a complex network. MCCE cannot make large conformational changes, but it does bring the protonation states into equilibrium with the input structure. Importing multiple snapshots from MD trajectories (each run with fixed protonation) to MCCE allows the method to see the effects of backbone movements.

In MCCE a protonation microstate gives the protonation state of each residue in the protein [56]. To study PLS, MC sampling provides the probability of accepted proton distributions and how these changes when the input structure changes. This procedure has been used to

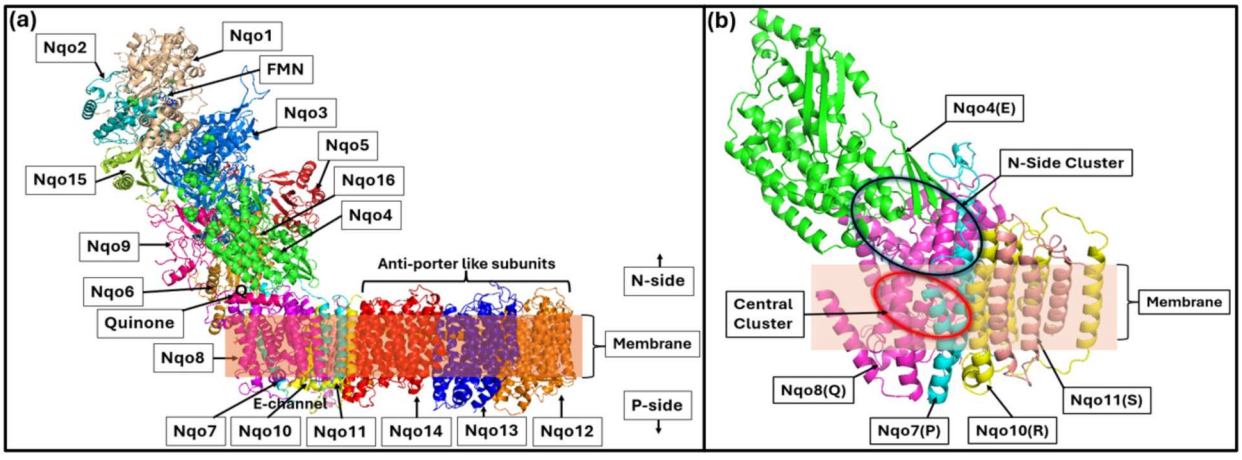


**Fig. 1.** (a) Full Complex I coordinate taken from MD snapshot, with membrane and surrounding waters removed. The iron-sulfur clusters, and buried water molecules shown. (b) Five subunits extracted from the complete Complex I are used in MCCE simulation. Nqo numbers give the subunit identifiers used for the *T. thermophilus* Complex I and letters (E, P, Q, R, K) are the chain ID in the PDB file used (PDB ID: 4HEA). The region of the N-Side and Central clusters (Fig. 2) are in the oval regions. Table S1.1 provides translation to subunit identifiers used for Complex I from other organisms.

investigate the PLS of the b-type CcO as well as in the quinone loading site in bacterial photosynthetic reaction centers [55,56].

Here, we explore the PLS in the *E*-channel of *T. thermophilus*. The study relies on an earlier identification of clusters of amino acids that are highly interconnected, leading across the protein from N- to P-side [10]. Sparse hydrogen bonds connection link the clusters. The hypothesis explored here is that a cluster of residues can form a PLS. MCCE is used to calculate the Boltzmann distribution of protonation microstates in the *E*-channel in multiple snapshots from MD trajectories carried out with menaquinone (MQ) and menaquinol ($MQH_2$) bound or with the apo-protein. A cluster on the N-side and another in the protein core are found with different net charges in different snapshots, indicating each can bind and release a proton to serve as a PLS. Each PLS couples protonation changes of residues separated by many Ångstroms. The microstate analysis allows us to determine which residues bind protons. Each PLS has multiple tautomeric states, where the cluster has the same net charge but different proton distributions. There is a strong anti-correlation of proton binding to the N- and P-side clusters. The central cluster tends to load protons when quinone is bound while the N-side cluster is more likely to be loaded in snapshots from the apo or $MQH_2$ bound trajectories.

## 2. Methods

### 2.1. Preparation of the structure for MCCE

The calculations start with the *Thermus thermophilus* apo-Complex I crystal structure (PDB ID: 4HEA) at 3.3 Å resolution [51]. MQ and $MQH_2$ bound structures were generated by docking the decyl ubiquinone from the structure 6I0D into the 4HEA structure, modifying the head group and then relaxing the loop from Nqo6 [55–70] (see SI.1.1 for details). The parameters for Iron-sulfur clusters are taken from Density Functional Theory calculations by Chang and Kim [58] Iron-sulfur clusters N1a, N1b, N5, N7, and N6b ware oxidized while N3, N4, N6a, and N2, reduced. This choice is based on studies of bovine Complex I [59–61]. The parameter set for Flavin mononucleotide are from Freddolino et al. [62]. Each trajectory is 0.5 microsecond long [10]. The trajectories used here were previously used in earlier studies of the *E*-channel proton transfer pathways [10] and the motions and orientation of the protein [51,53].

Unfortunately, there is no consensus identification for Complex I subunits from different organisms. Here, subunits are identified using the *T. thermophilus* numbering. Table 2 and Table SI.1 provide the translation to the chain designations in the 4HEA PDB file.

Snapshots were selected for MCCE input in several ways. Every 10th snapshot in each trajectory was subjected to MCCE analysis. Following the MCCE calculations, we identified regions within the MD trajectories where the proton binding stoichiometry changed. Snapshots were added to include more examples with different proton loading. Additionally, snapshots from each trajectory were binned using the MDanalysis [63,64] and TTClust [65] programs, based on varying residue distances. More snapshots were added to ensure that each structural class was represented. MCCE simulations were subsequently performed on 40 snapshots from the MQ, 20 from the $MQH_2$ and 20 from the apo-trajectories. While the different snapshots do have different distributions of protonation states, no significant movements of the helices were observed, and the backbone RMSD values are below 0.9 Å.

### 2.2. MCCE calculations on the E-channel

MD simulations are carried out on the full membrane embedded apo, MQ and $MQH_2$ bound Complex I [51]. For MCCE calculations of the E-channel, only the subunits Nqo4, 7, 8, 10 and 11 are included (Fig. 1). All MD water molecules and membrane are removed, A 30 Å low-dielectric rectangular region is created to mimic the hydrophobic portion of the membrane using the IPECE program (See SI.1.2) [66]. The system is surrounded by a continuum solvent with a dielectric constant of 80 with 150 mM salt and the protein is given a dielectric constant of 4. Interior cavities are filled with implicit water with a dielectric constant of 80.

The MCCE calculations use the 'isosteric' conformer choices. The backbone position is fixed given the MD snapshot input. MCCE samples the ensemble of states that differ in the protonation state of Asp, Glu, Tyr, Cys, Arg, His and Lys, and hydroxyl orientation, neutral His tautomer and Asn, Gln side chain amide orientation [57,67]. The MCCE calculations are identical to those used for the analysis of the *E*-channel hydrogen bond network with one exception. Previously explicit water molecules were retained from the MD snapshots as they are essential to complete the proton transfer paths [10]. Here, implicit water is used as this provides a more reproducible calculation of protonation states with less computational effort [66]. SI.1.3 provides additional details about the MCCE force field.

### 2.3. Microstate analysis

MCCE makes side chain and ligand conformer choices for position and charge states. A microstate, which is one conformer choice for each group, is subjected to Metropolis-Hasting MC sampling (See SI.1.4 for additional details). All accepted microstates are saved for analysis [56]. Protonation microstates define the charge of each acidic and basic residue [56]. A given protonation microstate can exist in numerous conformations. Protein tautomers are protonation microstates with the same total charge but different proton location [56].

### 2.4. Energy difference between states with different net charge

The free energy difference between any two states can be obtained if we know their probability in the Boltzmann ensemble. Here the probability of all tautomers, i.e. microstates with the same charge, are combined. The free energy difference for a cluster of residues in microstates with an extra proton bound (loaded) or unbound (unloaded) is:

$$\Delta G = -1.364\, log_{10}\frac{(Count)_{loaded}}{(Count)_{unloaded}} \quad (2)$$

Here, $(Count)_{loaded}$, is the total count of accepted microstates with an extra proton bound, and $(Count)_{unloaded}$, is the total count of those with one fewer proton. The unloaded state is the reference here and this calculation is carried out given the microstate distribution for MCCE calculations from a single MD snapshot.

## 3. Results

The goal here is to identify which residues bind and release protons, acting as the PLS in the *E*-channel in Complex I to help untangle the proton transfer mechanism. All proteins will be found in a mixture of states. MCCE provides a unique MC method, analyzing all residue protonation states [68]. It uses Monte Carlo sampling to generate the Boltzmann distribution of protonation states that should be found in a real protein preparation. The PLS are then identified as clusters of residues that have different protonation states in different reaction intermediates, here modeled by individual MD snapshots. MCCE shows how residue protonation changes are coupled together.

### 3.1. Microstate energy distribution

#### 3.1.1. Many protonation microstates are found in the E-channel

While the entire protein is included in the MD trajectory, the MCCE calculations only consider subunits Nqo4, Nqo7, Nqo8, Nqo10, and Nqo11, which form the unique E-channel (Fig. 1b). These subunits contain 1135 residues with 224 protonatable residues (Asp, Glu, Tyr, His, Lys, Arg). In an MCCE calculations of a representative MQ-docked

snapshot at pH 7 there are >600,0000 unique conformation/protonation microstates accepted. In solution, at pH 7 Asp, Glu, the C-terminus, Lys and Arg would be ionized with neutral Tyr and His and the N-terminus in a mixture of charge states. Here, 74 of the residues are found to not be in their 'expected' charge state in accepted microstates and many are in different protonation states in different microstates. There are >25,000 unique accepted protonation microstates, with ~240 making up 50 % of the total ensemble and ~ 8000 needed to contain 90 % of the total (Table 1 and Table SI.3). Thus, MCCE finds the protein has many protonation states that are close in energy so would be found in the equilibrium ensemble. Each MD snapshot provides a similar picture.

Fig. 3a shows the distribution of >25,000 protonation microstates in one frame from the MQ-trajectory (Table 1). Each dot is a unique protonation microstate. The dots in a column are tautomers, sharing the same charge but with different residues protonated. Some protonation microstates are found >100,000 times while others are accepted <10 times. In a microstate, each protonatable group has a defined charge of 0 or ± 1, so microstates have integer charges. Accepted microstates in the *E*-channel have charges ranging from −9 to +3 with the most probable charges between −2 to −4 (Fig. 3a). The Boltzmann averaged ensemble is formed of microstates with different charges so has a non-integer value. The ensemble average charge for this representative snapshot is −3.2. The complex mixture of protonation states qualitatively changes little between snapshots (Fig. SI.1). However, we will see that dividing the protein into interconnected groups reduces the problem to one where clear differences can be seen in the equilibrium mixtures in different snapshots, identifying PLS loading and unloading.

### 3.2. Central Cluster loaded and unloaded states

#### 3.2.1. The proton transfer network identifies residue clusters

Previous mapping of the proton transfer paths through the *E*-channel in MD snapshots identified six clusters of highly interconnected residues (Fig. 2) [10]. Residues in clusters are each connected to at least 6 other residues either directly or through four or fewer water molecules in different MCCE conformation/protonation microstates. Clusters are then connected by a few hydrogen bonds. The clusters form natural regions to be analyzed independently. The hypothesis is that the protonation states will come to equilibrium in each highly interconnected cluster. Proton transfer between clusters can be gated by the limited inter-cluster connections. We find that only a modest number of protonation microstates will describe each cluster (Table 1).

On the N-side there is a cluster surrounding the quinone binding site (cluster 1 [10]) with 11 residues (Fig. 2a). This is flanked by two clusters connected to the surface (clusters 2 and 3) with 37 residues (Fig. 2a) [10]. These three clusters will be grouped together as the N-side cluster. The N-side cluster is linked to the 26 residues in the deeply buried Central Cluster (cluster 4) (Fig. 2a). A smaller, isolated cluster 5 was identified. The P-side exit cluster (6) has 32 residues, including several exposed on the P-side surface. The proton path was found to extend from the quinone binding site through the Central Cluster, with rare connections to the P-side exit cluster.

**Table 1**
Census of residues and microstates in *E*-channel.

| | Average 10 snapshots | | |
|---|---|---|---|
| | E-Channel | Central Cluster | N-side cluster |
| Number Asp, Glu, His, Tyr, Arg, Lys | 224 | 15 | 30 |
| Number residues changing charge | 74 | 6 | 5 |
| Average charge | −3.2 ± 0.5 | −1.5 ± 0.1 | −3.4 ± 0.1 |
| Count of accepted protonation microstates | | | |
| All | 25,402 ± 970 | 36 ± 10 | 25 ± 5 |
| 90 % of ensemble | 8200 ± 126 | 7 ± 2 | 3 ± 0 |
| 50 % of ensemble | 247 ± 56 | 2 ± 0 | 1 ± 0 |

MCCE calculated microstates in 10 representative MQ-docked snapshots with the Central Cluster average charge of −1.49 and thus in a mixture of loaded and unloaded microstates at pH 7. Residues in the Central and N-side Clusters were identified in the previous analysis of the proton transfer paths, that change charge in different microstates [10]. The active residues in the Central and N-side Clusters are listed in Table 2 and all cluster residues in Table SI.2. See Table SI.3 for results from different snapshots.

#### 3.2.2. The Central Cluster net charge

The Central Cluster has seven acidic residues (Asp, Glu), three bases (Lys, Arg, His), thirteen Grotthuss competent residues (Ser, Thr, Tyr) and three Non-Grotthuss polar residues (Asn, Gln, Trp) (Table 2 and Table SI.2). All these residues are buried. MCCE is carried out on multiple snapshots extracting the five *E*-channel subunits. First the average net charge is determined for the Central Cluster in each snapshot. The Central Cluster charge in snapshots from the MQ docked trajectory ranges from −2.08 to −1.00 (Fig. SI.2a). Thus, different snapshots have different proton affinities. The non-integer cluster net charge reflects the distribution of individual microstates with different charges. Those with a charge near −2 have mostly unloaded microstates (Fig. 2d); those with a net charge near −1 mostly have microstates with a proton bound (Fig. 2b); and the snapshot with a cluster charge of −1.49 has a nearly equal mixture of loaded and unloaded microstates in the ensemble (Fig. 2c). To identify snapshots, those with an average charge from −2.08 to −1.80 are considered unloaded; −1.29 to −1.00 are loaded and those with a net charge from −1.79 to −1.30 are mixed loaded-unloaded (Fig. SI.2a).

Each trajectory has a different proportion of snapshots with different degrees of proton loading. The Central Cluster is almost always unloaded in snapshots from trajectories with an empty quinone site or with $MQH_2$-bound. A few snapshots are classified as mixed loaded and unloaded, but no snapshot has mostly loaded microstates. In contrast, the trajectory with MQ bound has a similar number of snapshots that are mostly loaded, mostly unloaded, or with a mixture of loaded and unloaded microstates (Fig. SI.2a).

The energy difference between the proteins in different charge states can be determined given the relative probability of microstates of different charges (Eq. 2). We can see here the system is not very deeply trapped with or without a proton bound. The free energy difference between states with −1 or − 2 net charge is only 1.4 kcal/mol for the snapshots defined as being loaded and 1.9 kcal/mol for those designated unloaded (Table 3).

#### 3.2.3. Central Cluster PLS protonation microstates: Tracking the proton movement

The unique Central Cluster residue protonation microstates were found. Here all conformations and protonation microstates of other residues are counted in one group as long as the Central Cluster residue protonation states are the same. By restricting the analysis to the 15 Central Cluster protonatable amino acids we avoid the combinatoric explosion (Fig. 2b, c, d). Now there are 30–40 unique protonation microstates for the Central Cluster. Only 4–5 microstates make up 90 % of the ensemble (Table 1 and Table SI.3).

In the Central Cluster Lys and Arg are always ionized, and Tyr is always neutral. Thus, only six Central Cluster residues 8-E163, E130, E213, and H251, and 7-D72, and E74 have different protonation states in the accepted microstates (prefix is the Nqo subunit number) (Table 2). Microstates are found with a charge ranging from −4 to 0 (Fig. 3b-d). Those with the charges −1 and − 2 are the most probable and are considered to be loaded and unloaded.

We will describe here the results from three representative snapshots, one mostly unloaded (charge −1.99), mostly loaded (−1.11) and one mixed loaded-unloaded (−1.49) (Fig. 3b, c, and d). The microstates described here predominate in 85 % of snapshots (Fig. 4c), however their exact probabilities vary. Some snapshots do have other microstates

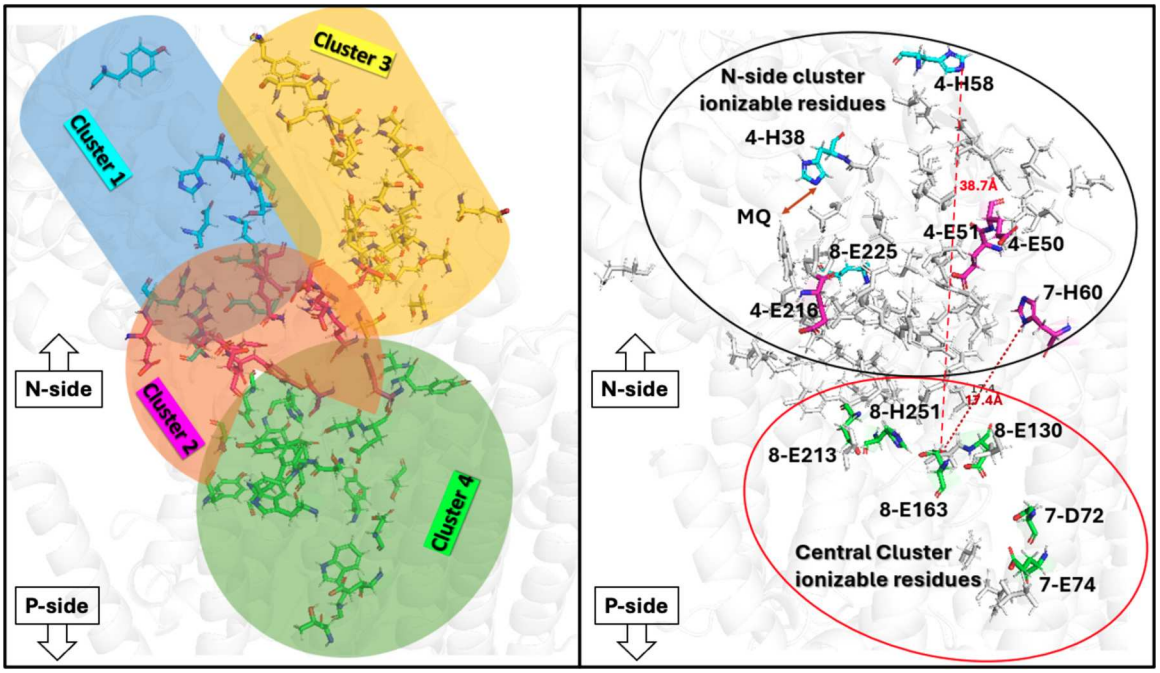


**Fig. 2.** (a) All the cluster residues from a comprehensive analysis of the *E*-Channel H-bond network by Khaniya et al. [10]. Different colors show the cluster regions (cluster numbers 1–6 as assigned there): N-side Cluster: (1: cyan; 2: magenta, 3: yellow) and Central Cluster (4: green). Not shown: P-side cluster (cluster 6) below the Central Cluster and Cluster 5: between Cluster 3 and 4. (b) Residues that are active in PLS proton binding and release in: Top Circle: N-side cluster; Bottom Circle: Central Cluster. Residue labels: *T. thermophilus* subunit number designation, one letter amino acid code, residue number. Residues that are shown to change protonation in the extended PLS are labeled. See Table SI.2 for list of all residues in each cluster. (For interpretation of the references to colour in this figure legend, the reader is referred to the web version of this article.)

**Table 2**
Residues loading and unloading protons in the Central and N-side clusters in Nqo4, 7, and 8.

| Cluster name | Active residues | *T. thermophilus* Subunits (4HEA chain ID) |
|---|---|---|
| Central cluster | D72, E74 | Nqo7(P) |
| | E163, E130, E213, H251 | Nqo8(Q) |
| N-side cluster | H38, E50, **E216**, **E51**, **H58** | Nqo4(E) |
| | H60 | Nqo7(P) |
| | E225 | Nqo8(Q) |

Active residues change protonation in different microstates. One letter amino acid code plus residue ID. The underlined residues in the N-side cluster are surface exposed and bold residues are in the quinone containing, peripheral domain. All Central and N-side cluster residues from reference [10], including those that have the same charge in all accepted microstates, are reported in Table SI.2.

at high probability, which are shown in Table SI.4. The ensemble for each snapshot includes microstates with different net charge, as expected given the modest free energy difference between loaded and unloaded states (Table 3). For example, in the loaded frame the three highest probability microstates have a net charge of −1. Microstates with a charge of −2 and even −3 and 0 are found with low probability (Fig. 3b). In the unloaded frame, microstates with a −2 charge represent 90 % of the total (Fi. 3c). The mixed loaded-unloaded frame has an ≈50:50 loaded-unloaded microstates with a −1 and −2 charge (Fig. 3d).

Fig. 4 describes the predominant Central Cluster microstates in three snapshots. The Central Cluster extends over 24 Å from 8-E213 near the N-side to 7-E74 nearer the P-side (Fig. 4b). A schematic indicates the location of the proton in each microstate with an asterisk identifying sites with a proton. The net microstate charge as well as its probability in the full ensemble are provided. In unloaded frames either or both the P-side residue 7-D72 and 7-E74, which are within 5.0 Å of each other, are deprotonated (Fig. 4c). In loaded states a proton is almost always bound by both acids (Fig. 4). In contrast, the mixed loaded-unloaded snapshots tend to bind protons nearer the N-side on 8-E163 and 8-E130 (Fig. 4). Thus, the loaded Central Cluster stabilizes protons nearer the P-side of the extended cluster, poising them for release.

### 3.3. Correlation of Central Cluster residue protonation

One significant advantage of having access to all microstates lies in the ability to uncover correlations amongst residues. The Pearson weighted correlation of protonation states of the Central Cluster residues was determined (SI. Eq. 1) [56]. A positive correlation shows groups that are more likely to be ionized simultaneously, whereas a negative correlation indicates that the ionization of one group decreases the likelihood of the other group being ionized (see SI.1.5). All the active groups in the Central Cluster influence each other. Residue 8-E163 is pivotal, as its ionization is negatively correlated with 7-D72 and 8-E130 and positively correlated with 8-H251 (Fig. 5). Likewise, 8-H251 is positively correlated with 7-D72 and 7-E74. Thus, a proton tends to be on the His on the N-side or 24 Å away on one of the P-side acids. This highlights the long-range coupling within this cluster. The correlation coefficient is never close to one, indicating that these correlations are preferences rather than rules. Correlation analysis for loaded and unloaded snapshots can be found in Fig. SI.2.

The two adjacent P-side acids, 7-D72 and 7-E74 are 5 Å apart from each other. 7-D72 has been previously discussed as part of a PLS [9,19,28,54,69]. Here we find that both contribute, and their ionization is anticorrelated (Fig. 5 and Fig. SI.3). They are both predominately neutral in loaded structures; however, 7-D72 and 7-E74 have similar probability of being ionized in higher energy microstates (Fig. 4). In the mixed loaded-unloaded snapshots 7-E74 is more likely to be ionized, whereas in the fully unloaded snapshots 7-D72 is more likely to be ionized with 7-E74 retaining the proton.

**Table 3**
Average free energy of proton binding in Central Cluster (Kcal/mol).

| | | Microstate charge | | | | | |
|---|---|---|---|---|---|---|---|
| | | 0 | −1 | −2 | −3 | −4 | |
| Frame Types | Avg. Charge | Central Cluster Microstate relative free energy | | | | | Number of snapshots |
| Loaded | −1.10 | 3.2 ± 0.9 | **−1.4 ± 0.5** | 0 | 3.8 ± 0.8 | >7 | 12 |
| Mixed | −1.49 | 5.0 ± 0.8 | 0.3 ± 0.2 | 0 | 3.1 ± 0.9 | 5.6 ± 1.5 | 12 |
| Unloaded | −1.99 | 5.5 ± 0.9 | 1.9 ± 0.3 | 0 | 2.5 ± 0.9 | 6.3 ± 1.2 | 9 |

Snapshots with net charge of Central Cluster residues 8-E213, 8-H251, 8-E130, 8-E163, 7-D72, and 7-E74 from −2.08 to −1.80 are unloaded; −1.29 to −1.00 are loaded and those with a net charge from −1.79 to −1.30 are mixed loaded. The state with a − 2 charge is the reference state. The energies are calculated given the population of microstates with each charge in the ensemble using Eq. (2). The lowest energy state is underlined. The relative free energies are calculated for individual snapshots and these results are averaged.

### 3.4. The N-side Cluster

Three clusters were identified in the analysis of the H-bond networks close to the N-side of the *E*-channel, previously designated clusters 1, 2, and 3 [10] (Fig. 2). There are five Asp, nine Glu, one Lys, six Arg and three His in the combined N-side cluster (Table SI.2). All Arg and Lys remain ionized and Tyr neutral. There are six residues that change charge: 4-E58, 4-E51, and 4-E216 in the peripheral arm and 4-E50, 8-E225, and 7-H60 which are just above the membrane surface (Fig. 2, Table 2).

Residues 4-H38, 4-D139, and 4-H58, which are in the hydrogen bonded N-side cluster, are not included in the N-side cluster charge. While these residues can be connected via hydrogen bonds to the other residues, they are far from the membrane and thus less likely to inject protons into the E-channel. MQ is bound to 4-Y87 and 4-H38, while 4-D139 is bound to 4-H38 [54,70–72]. The Asp 4-D139 is always ionized and 4-Y87 neutral. The residue 4-H58 is ≈40 Å further away from the membrane in the periplasmic arm (Fig. 2b). While 4-H38 and 4-H58 do change protonation in our analysis, their ionization is not correlated with each other. The correlation of 4-H38 and the other N-side cluster residues is discussed below.

#### 3.4.1. The N-side Cluster net charge

The average N-side cluster charge varies between −3.8 and −2.6 in

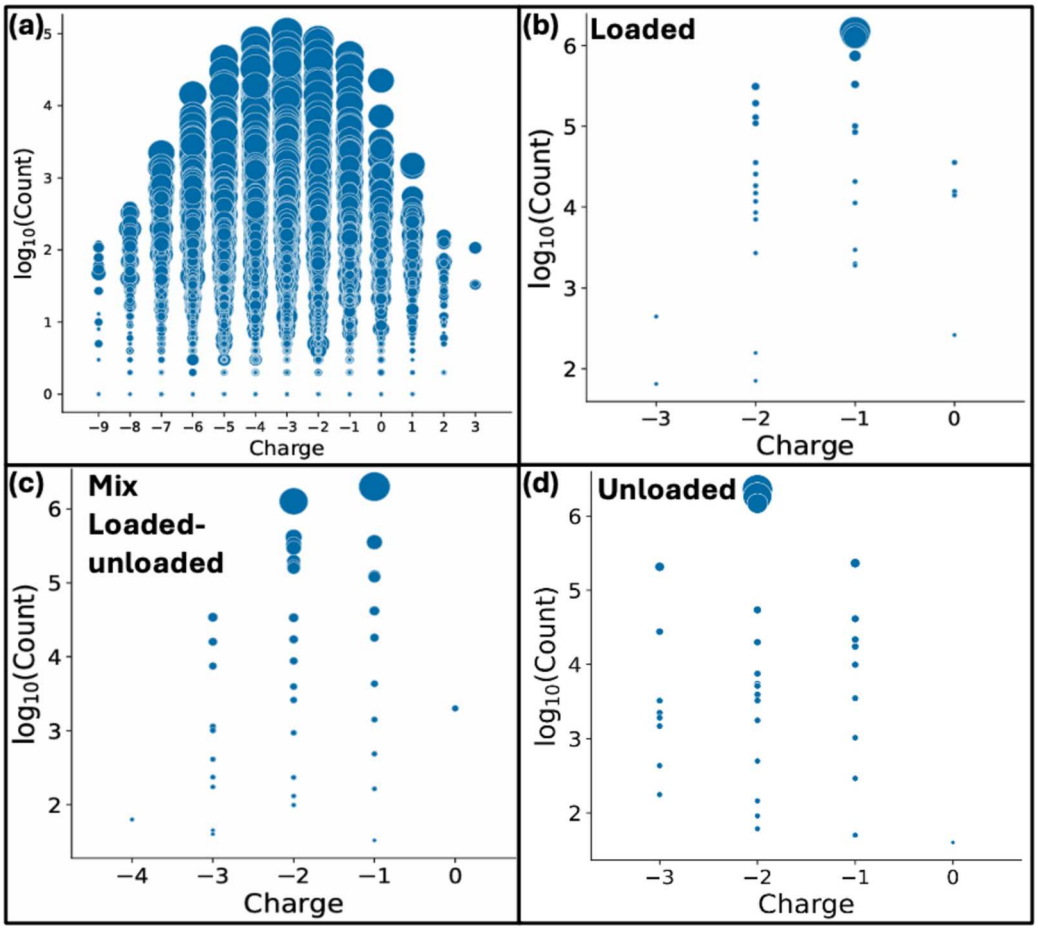


**Fig. 3.** Distribution of unique protonation microstates for three snapshots chosen by the net charge of the Central Cluster residues. Each dot gives the probability as $\log_{10}$(count) vs. the summed charge of that protonation microstate. Dots in a column are protein tautomers. Dot size indicates the range of energies of the conformational microstates that are found in this protonation state. (a) Five *E*-channel subunits, average ensemble total charge of −3.2. (b-d) Distribution of microstates for six Central Cluster residues in snapshots with average net charge of (b) −1.10 (loaded), (c) −1.49 (mixed loaded-unloaded), and (d) −1.99 (unloaded).

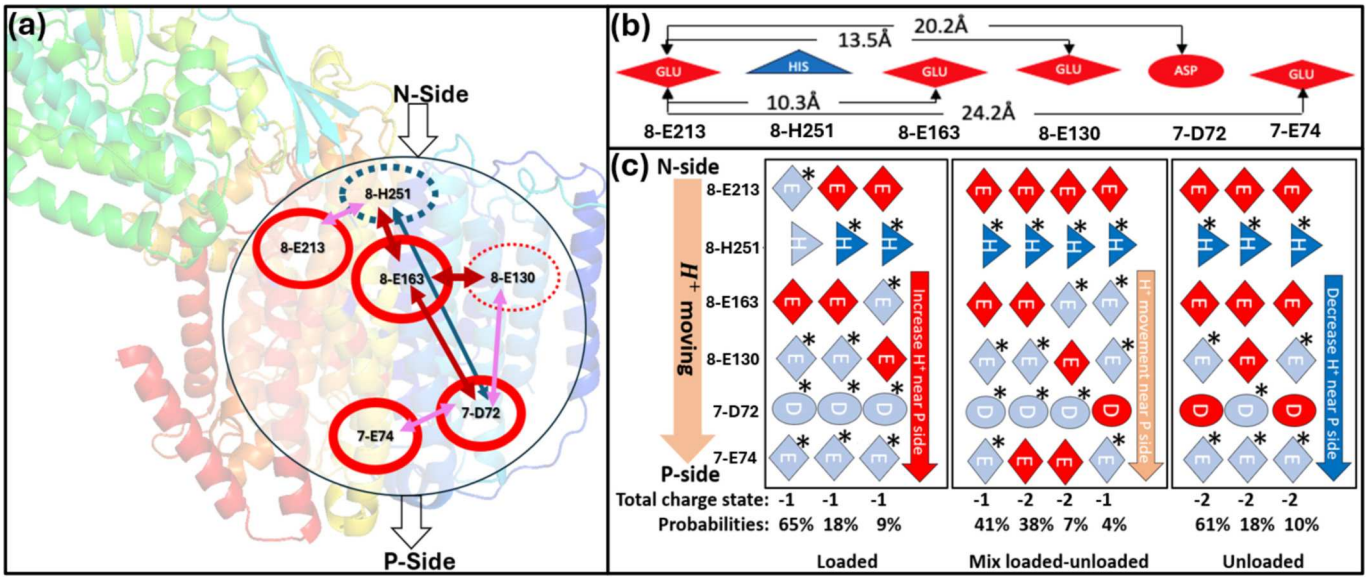


**Fig. 4.** Protonation of the Central Cluster active residues in microstates from loaded, mixed and unloaded snapshots. (a) The Central Cluster residues whose protonation states differ in high probability loaded and unloaded microstates. The arrows indicate the coupling between the residues (Fig. 5). Red arrow: Negatively correlated protonation changes (when one residue is more ionized the other is less); Blue arrow: positive correlation. Arrow thickness indicates correlation strength. Circles around residue number reflect residue conservation in a multiple sequence alignment (Fig. 8). Solid: highly conserved; dashed: lower conservation. Red circles: acids; Blue: bases. (b) Distances between the residues. (c) Most probable protonation microstates found in MCCE analysis of a snapshot where the Central Cluster is loaded (left), mixed loaded-unloaded (middle) and unloaded (right). The microstates are shown vertically from the N- to the P-side (shapes: diamond: Glu, oval: Asp, triangle: His) Dark red: $Glu^-$ or $Asp^-$; dark blue: $His^+$; Gray: neutral. * Protonated residue. (For interpretation of the references to colour in this figure legend, the reader is referred to the web version of this article.)

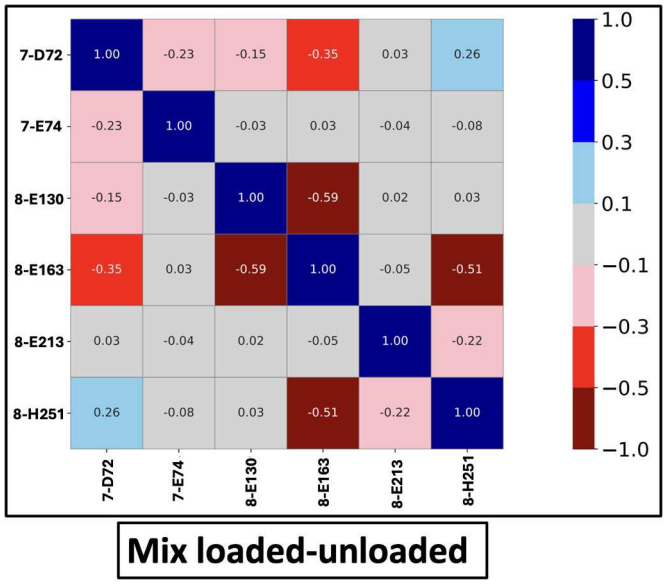


**Fig. 5.** Pearson weighted correlation coefficient (SI. Eq. 2) for Central Cluster residue protonation in a mixed loaded-unloaded snapshot. Only residues with an absolute correlation value ≥0.1 with at least one other residue are included. Each square gives the correlation strength between two residues. The colour denotes correlation values: dark red (−1.0 to −0.5), red (−0.5 to −0.3), pink (−0.3 to −0.1), light gray (−0.1 to 0.1), sky blue (0.1 to 0.3), blue (0.3 to 0.5), and dark blue (0.5 to 1.0). The correlations shown here are the source of the weight and colour of the arrows in Fig. 4a. (For interpretation of the references to colour in this figure legend, the reader is referred to the web version of this article.)

different snapshots, identifying it as a second PLS. A loaded cluster has a charge of −3 while it is −4 in the unloaded state (Fig. SI.2b). The large negative charge is supported by the positive electrostatic potential from the remaining protein. The N-side cluster charge in MQ trajectory snapshots ranges from −3.8 to −2.9 indicating some snapshots are loaded and others unloaded (Fig. SI.2b). The $MQH_2$ and Apo trajectory snapshots are mostly loaded with the total charge between −3.1 and −2.7 in the apo and − 2.9 and − 2.6 in the $MQH_2$ trajectory. This implies the proton-donating residues in the Complex I PLS get protonated while $MQH_2$ still remains bound to the cavity. The distribution of snapshots with different average charges is shown in Fig. SI.2b.

### 3.4.2. *N-side cluster PLS protonation microstates track the proton*

There are five N-side cluster residues whose protonation states differ in highly probable microstates. In the highest probability unloaded microstate, which makes up 61 % of the representative unloaded snapshot, none of five has a proton (Fig. 6b). In the most probable loaded microstates 7-H60, the residue closest to the Central Cluster, is protonated (Fig. 6a). Lower probability loaded microstates have the proton on either 4-E216, 4-E50 or 4-E51. There is less correlation amongst the protonation states of the N-side residues than was found for those in the buried Central Cluster PLS. The strongest correlation is between 4-E50 near the N-side surface and 7-H60, which is the residue closest to the Central Cluster (Fig. SI.4).

### 3.4.3. *Correlation between proton loading in the Central and N-side Clusters*

The average charge of the Central and N-side clusters was compared for each individual snapshot. Protonation of the two clusters is strongly anti-correlated (Fig. 7). In snapshots from the $MQH_2$ trajectory the N-side cluster tends to be loaded, and Central Cluster unloaded. Snapshots from the Apo and MQ trajectories are more diverse showing a range of loading for the two PLS, with the apo snapshots favoring a more loaded N-side cluster. On average the two PLS together hold on average ~ 0.9 protons. There are however a small number of snapshots where there are 1.2 to 1.4 protons loaded between the N-side and Central Clusters.

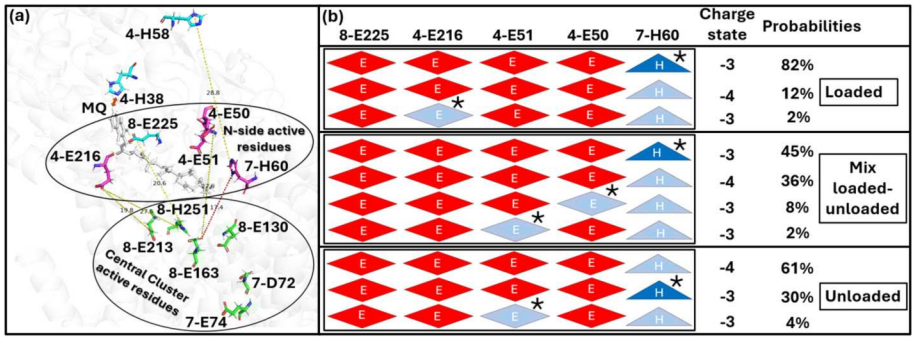


**Fig. 6.** N-side cluster protonation microstates. (a) N-side and Central Cluster active residues. (b) Most probable protonation microstates found in representative snapshot with N-side cluster loaded (top), mixed loaded-unloaded (middle) and unloaded (bottom). The microstates are shown horizontally with the same residue shape and colour designation found in Fig. 4.

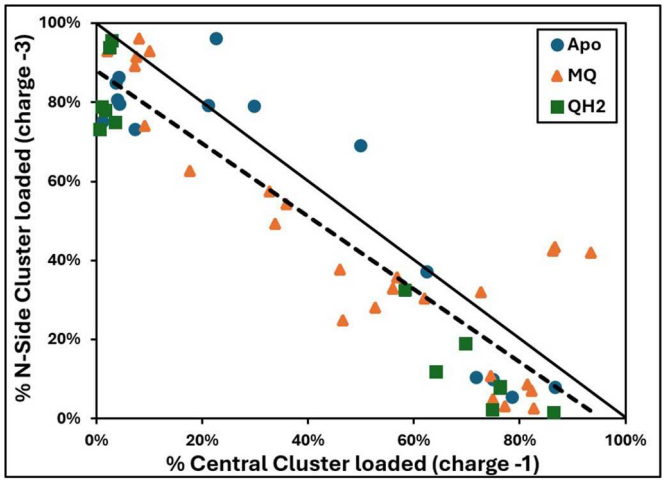


**Fig. 7.** Correlation of Central and N-side PLS proton loading. A dot shows the percentage of loaded Central Cluster microstates (charge state: −1) vs. N-side cluster (charge state: −3) in individual snapshots from the Apo (blue), MQ (orange), and $MQH_2$ (green) MD trajectories. Dashed line: Best fit slope −0.92 and $R^2$ 0.82; Solid line: y = −x. (For interpretation of the references to colour in this figure legend, the reader is referred to the web version of this article.)

### 3.5. Other buried clusters

#### 3.5.1. Second buried cluster

A small cluster, designated cluster 5, was identified in the study of the proton transfer paths. There were no connections between this cluster and any other cluster even when additional water molecules were added to aid connectivity [10]. The three ionizable residues in the cluster are 10-E32, 8-Y43 and 8-Y59. Only 10-E32 changes charge in the different snapshots, especially in snapshots from MQ and apo trajectories. It is mostly neutral in those from the $MQH_2$ trajectory. However, its ionization is not correlated with the Central Cluster charge (Fig. SI.5).

#### 3.5.2. The P-side cluster

The Central Cluster is 25 Å from the P-surface. A P-side cluster, which is largely parallel to the membrane surface, was identified. Only very rare connection were found between the Central and P-side cluster in the study of the proton transfer paths [10]. The total charge of the cluster is −1 and rarely changes in our simulation, even when we look at low probability microstates. The constant charge of the cluster indicates the alternative protonation microstates are >6 kcal/mol higher in energy. However, there are fluctuations in the ionization of 10-E5 or 8-K190 in several apo state snapshots. These changes either lead to low probability cluster binding or releasing of a proton.

### 3.6. Interaction of 4-H38 and 4-D139 in the MQ binding region

The residue 4-H38 is a ligand to the MQ and can make a hydrogen bond to 4-D139. A break of the His-Asp hydrogen bond on quinone reduction has been proposed as a trigger for proton pumping [54]. The parent structure, 4HEA, has them close together. In the apo trajectory, the pair maintain a short distance of ~2.6 Å until the last frames where they begin to move apart (Fig. SI.6a, and c). In the $MQH_2$ trajectory the pair quickly move to be ~4.7 Å apart. In the MQ-trajectory the distance between the His and Asp starts near ~2.3 Å and fluctuates, expanding beyond 8 Å.

During all MD trajectories, His is fixed neutral and Asp ionized (Fig. SI.6). The MD trajectory likely stabilizes these states. However, the His does take different charge states in the MCCE calculations, while the Asp remains ionized. In the MCCE analysis of $MQH_2$ snapshots, where the distance between the pair is intermediate and stable, the His is almost always neutral, perhaps as the nearby $MQH_2$ is protonated. In contrast, in the Apo snapshots, the Asp-His distance remains short, and the average His ionization in different snapshots ranges from zero to 60 % ionized, as there is no quinone for it to interact with. The distance varies in the MQ trajectory. The His is largely ionized when it is closest to the Asp so that it can form a hydrogen bond to both quinone and the ionized Asp; while it is more likely to be neutral when separated from the Asp. However, the correlation of ionization with distance is modest.

## 4. Discussion

Proton pumps require proton transfer paths connecting PLS, which are sites for temporary loading and unloading of protons. Here we examined the proton loading behavior of highly interconnected regions along the previously identified [10] proton transfer path through the *E*-channel in Complex I. The assumption underlying this study is that proton distribution within each cluster will be at equilibrium with the structure. Implicit assumptions are that protons bound to sites off the path will not be transported so they cannot be part of PLS; and that gating can be achieved either by breaking the sparser inter-cluster connections or by making the PLS proton affinity so high or low that protons cannot move through it [21].

### 4.1. Residues in the PLS

Analysis of the Boltzmann distribution of microstates generated in MC sampling shows a mixture of high probability protonation microstates. We found two PLS, each with residues stretching over many Ångstroms. Thus, the PLS are not individual residues but rather each an extended, interconnected group of residues. The proton affinity of the cluster determines PLS loading. The loading of the two PLS are anti-correlated suggesting that a proton bound to the N-cluster may be transferred to the Central Cluster. Only about 10 % of the proteins do not

have a proton bound to either the N-side or Central Cluster PLS (Fig. 7).

There have been earlier studies that pointed to residues of interest in the E-channel identified by inspection of the structure plus consideration of residue conservation (Table SI.5) [6,9,13,19,20,41,42,54,69–71,73–75]. Some studies calculated changes in the average proton affinity of individual residues using traditional methods that deliver uncorrelated, individual site average protonation [6,9,13,19,20,41,42,54,69,71,73–75]. MC sampling allows an unbiased examination of all residues, identifying additional residues of interest (Fig. 2b). Comparison of individual protonation microstates shows how the proton can move from N- to P-side of the extended PLS clusters.

We find eight previously identified residues are involved in proton loading (Table 2 and SI.5) [6,9,13,19,20,41,42,54,69,71,73–75]. The MC analysis here identifies additional residues in the N-side cluster just above the membrane (Table 2). These residues form water molecule mediated, hydrogen bonds and change protonation in highly probable protonation microstates. The identification of the N-cluster as a PLS may support earlier computational analyses [19,54] that proposed the protonation states of Nqo7 Asp and Glu residues near the solvent interface as part of proton-conducting water molecule channels.

### 4.2. Complex vs simple pumping elements

Proton paths and their PLS are being found in two flavors. There are linear paths such as the D-channel in CcO [21,76] and the antiporter channels in Complex I [6,9,13,74,77]. These can be dominated by single isolated residue PLS, such as D132 and E286 at the entry and end of the CcO D-channel [15]. In the antiporters, a linear array of 4–5 protonatable residues form a PLS. Linear proton paths and simple PLS can be found by inspection of the structure. Mutation of a single residue greatly reduces pumping efficiency [37–39,75,78–80]. The residues along these paths are often highly conserved.

In contrast, complex proton transfer paths have a network of competing routes. The associated PLS are more often clusters of residues. Proton pumps seem to use both simple and complex paths. For example, while protons come in to CcO via linear paths they exit via a complex network on the P-side [21]. The hypothesis is that there are multiple ways to move a proton through the pump. Thus, multiple mutations that block alternative paths are needed to block activity. This is seen in the proton input path in bacterial reaction centers [55] and found for *E*-channel mutations (Table SI.5) [81].

### 4.3. Mutation and conservation of PLS residues

In Complex I the antiporter channels are simple while the E-channel is not. Experiments measured the rates of NADH oxidization or quinone reduction that are strongly coupled to proton pumping in mutants of *E. coli* or *P. denitrificans* Complex I. Mutation of individual residues identified here as contributing to the PLS led to diminished but not fully inhibited rates (Table SI.5) [75,81–83]. For example, 7-E163 appears as a key element in the Central Cluster PLS, but when it is mutated the rate of pumping coupled NADH oxidation is slowed by 75 %. However, multiple mutations are more lethal. For example, individual removal of 7-D72 or E74, inhibit activity but when both are changed to non-ionizable residues the reaction is 98 % inhibited [81] (Table SI.5).

### 4.4. Central cluster conservation

The conservation of the residues that form the Central Cluster PLS and the residues within 5.0 Å around them was determined (see SI.1.6). The coupled residues 8-E213, and 8-E163 near the N-side and 7-D72, and 7-E74 near the P-side are highly conserved (Fig. 8; top). This finding can support an important role for 8-E163 in different organisms (Fig. 4a). In contrast, 8-E130 is often a Ser and 8-H251 can be a variety of polar residues (Table SI.5).

The surrounding residues play two roles in proton transfer. Hydroxyl containing residues are Grotthuss competent; hydrophilic residues can help stabilize bound water molecules needed for proton transfer paths; and the electrostatic potential generated by the surroundings support the PLS loaded and unloaded charge states. The Central Cluster connects residues separated by over 22.0 Å. The multiple sequence alignment shows polar surrounding residues are often conserved. Overall, the residue types are usually maintained even when the residue identity is not (Fig. 8).

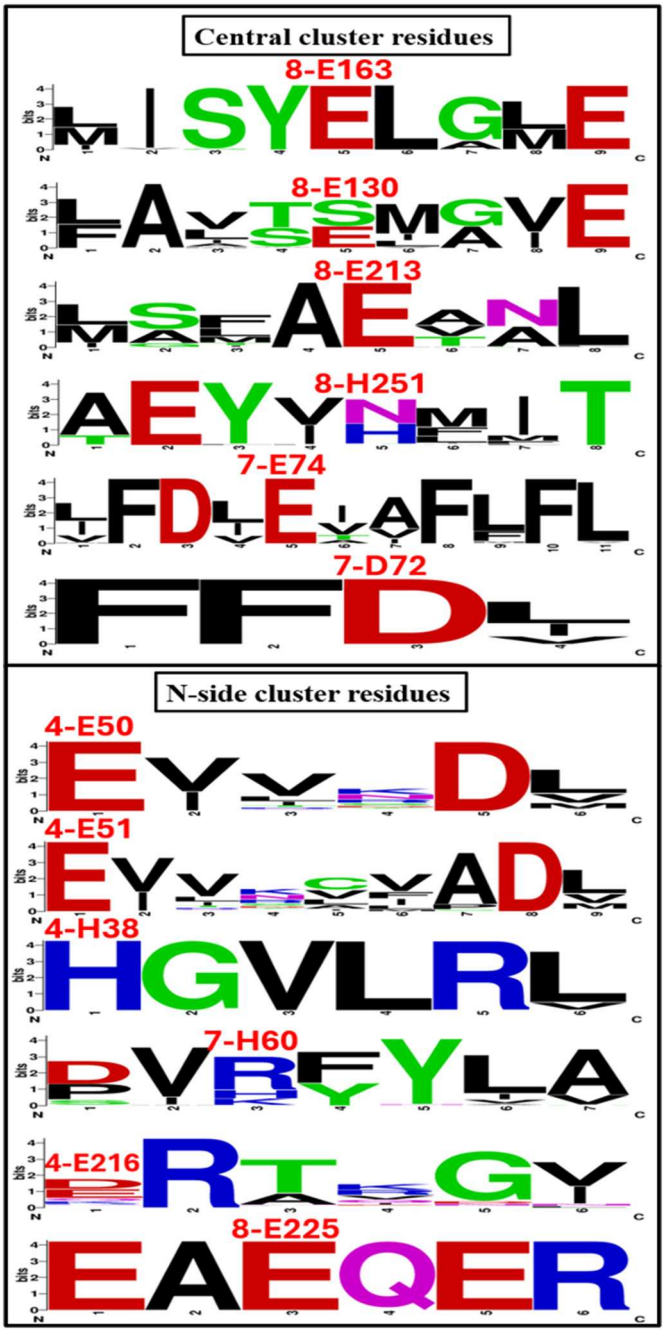


**Fig. 8.** Web-logo [84] representation of multiple sequence alignment of 1000 Complex I sequences for only residues within 5.0 Å of the active PLS residues in the Central Cluster and the N-side cluster. The surrounding residues in the Central Cluster and the N-side cluster are given in Table SI.6. These are in subunits Nqo4, Nqo7, Nqo8, Nq010, and Nqo11 in *T. thermophilus* Complex I. Residues name identified by *T. thermophilus* subunits Nqo4-, Nqo7-, and Nqo8- one-letter residue name, and followed by residues ID shown on top of each key residues. Their degree of conservation is the source of the circle type (thickness, solid or dashed) in Fig. 4a and Fig. SI.3.

### 4.5. N-side cluster conservation

In the N-side Cluster only 8-E225, 4-E51, 4-E50 and the quinone ligand 4-H38 are highly conserved while 4-H58, 7-H60 and 4-E216 are not (Fig. 8 and Table SI.5). Conservation of surrounding, non-protonatable residues is variable, with some well conserved and others not (Fig. 8; top).

### 4.6. Towards a unified model of pumping

It is challenging to imagine a mechanism that can couple electron transfer in the peripheral arm of Complex I with proton pumping through four channels. Models of pumping consider how the quinone reduction or movement influence the residues between the quinone site and the top of the *E*-channel, which are in the N-side cluster here [12,52,54,85–87]. Others consider the communication to the antiporter channels, via coupling through the adjacent ionizable residues in the membrane center [9,12,87–89]. Models of pumping through the E-channel have been proposed [11,52], while others suggest no protons are pumped through the E-channel [35].

Here we assume the E-channel pumps a proton. A model of pumping would connect the proton loading and the proton paths in the different intermediate states. The calculation of PLS loading presented here is carried out on the same trajectories as a previous study of the proton transfer paths (Fig. SI.7) [10]. Thus, we can compare the degree of connectivity with the loading of putative E-channel PLS described here.

Snapshots from the $MQH_2$ trajectory have the N-side cluster fully loaded, with little proton loading in the Central Cluster and few connections between the two clusters. The quinol would then be released. In the apo trajectory the proton has moved into the Central Cluster and this PLS continues to fill when MQ is subsequently bound. The rare connections to the P-side cluster are made in the apo trajectory, indicating this may be the state where protons would be released to the P-side. However, the Central Cluster is most highly filled when MQ is bound, which could also make this a good candidate for proton transfer to the P-side. There are multiple steps going from MQ to $MQH_2$ with a first and second reduction and quinone protonation being able to modify the loading of the clusters. Also the quinone or quinol may be transiently bound in different binding sites as it moves from the membrane into the periplasmic arm [85,86]. Thus, we do not have information about intermediate structures here and so can only provide this partial view.

It should also be noted that the calculations do not show the PLS strongly traps the proton. In all snapshots MCCE finds mixtures of loaded and unloaded microstates with only a few kilocalories separating them (Table 3). This may be simply due to the limitation of the MD snapshots. Alternatively, it may be a property of Complex I pumping if the strong physical gate found between the Central and P-side clusters ensures the proton only moves when the gate opening is triggered.

The P-cluster remains largely inert, keeping the same protonation state in all snapshots. Thus, microstates with different numbers of protons loaded are at least 6 kcal/mol above those at low energy. Another concern is that there is rarely a path between the Central and P-side cluster. However, pumps are designed to be closed to transport except when coupled to the redox reactions that power them. Thus, a pathway from the N-side to the P-side proton exit is not found in any structure or in most MD simulations of other proteins. For example, a 'lucky' CcO MD trajectory found protonation of the P-side PLS triggered the opening of a water molecule-filled cavity in the hydrophobic region near the bridging Glu286, which serves as a single residue PLS. Water entry lowers the Glu proton affinity by >5 kcal/mol allowing proton release as well as a connection between the N- and P-sides of the protein [24]. Similarly, in b-type CcO all crystal structures have an extremely high proton affinity for the P-side PLS cluster. MD changed the structure to lower the proton affinity so that the PLS could be characterized [21]. Thus, we posit that the gate opening from the Central to P-side cluster is rare and that our trajectories have a P-side cluster trapped in a single loaded state still missing the gate opened, PLS binding conformation.

## 5. Conclusion

While the antiporter subunit and peripheral arm of Complex I are related to other proteins [6,9,11,44,46,47,74,90] the *E*-channel is unique. This channel is challenging to study as there is no linear proton transfer path. MC sampling allows us to identify the many possible paths by mapping the network of hydrogen bond connections [10]. Here MC sampling is used to find and characterize highly interconnected clusters that function as PLS. To identify PLS, alternative structures are required that differ in their proton affinity. Here MD snapshots in apo, MQ and $MQH_2$ states were evaluated. Previously identified clusters were found to change charge. In a cluster at the N-side of the proton, five residues are coupled together to form a PLS. Six residues function in an extended Central Cluster PLS. A small disconnected buried cluster also binds and releases a proton. However, in the structures that are available, the cluster on the P-side of the protein is inert. Many of the residues found to be active in the PLS have been studied previously by site-directed mutation. As found in other complex proton transfer motifs single mutations have modest effects, while double mutations are more lethal. This supports the picture of a complex, robust pumping element where there are multiple alternative ways to travel.

## CRediT authorship contribution statement

**Md. Raihan Uddin:** Writing – review & editing, Writing – original draft, Visualization, Validation, Software, Methodology, Formal analysis, Data curation, Conceptualization. **Umesh Khaniya:** Writing – review & editing. **Chitrak Gupta:** Writing – review & editing, Resources. **Junjun Mao:** Resources. **Gehan A. Ranepura:** Writing – review & editing. **Rongmei Judy Wei:** Writing – review & editing. **Jose Ortiz-Soto:** Writing – review & editing. **Abhishek Singharoy:** Writing – review & editing, Resources. **M.R. Gunner:** Writing – review & editing, Software, Funding acquisition, Conceptualization.

## Declaration of competing interest

Marilyn Gunner reports financial support was provided by National Science Foundation. Marilyn Gunner reports financial support was provided by DOE. If there are other authors, they declare that they have no known competing financial interests or personal relationships that could have appeared to influence the work reported in this paper.

## Acknowledgements

Gunner, Uddin, and Khaniya acknowledge financial support from NSF MCB-2141824. Abhishek Singharoy and Chitrak Gupta acknowledge start-up funds from the SMS and CASD at Arizona State University, and the resources of the OLCF at the Oak Ridge National Laboratory, which is supported by the Office of Science at DOE under Contract No. DE-AC05-00OR22725, made available via the INCITE program.

## Data availability

Data will be made available on request.

## References

[1] P. Mitchell, Coupling of phosphorylation to electron and hydrogen transfer by a chemi-osmotic type of mechanism, Nature 191 (4784) (1961) 144–148, https://doi.org/10.1038/191144a0.
[2] J.P. Abrahams, A.G. Leslie, R. Lutter, J.E. Walker, Structure at 2.8 a resolution of F1-ATPase from bovine heart mitochondria, Nature 370 (6491) (1994) 621–628, https://doi.org/10.1038/370621a0.
[3] I.N. Watt, M.G. Montgomery, M.J. Runswick, A.G. Leslie, J.E. Walker, Bioenergetic cost of making an adenosine triphosphate molecule in animal mitochondria, Proc.

Natl. Acad. Sci. 107 (39) (2010) 16823–16827, https://doi.org/10.1073/pnas.1011099107.
[4] S. Iwata, J.W. Lee, K. Okada, J.K. Lee, M. Iwata, B. Rasmussen, T.A. Link, S. Ramaswamy, B.K. Jap, Complete structure of the 11-subunit bovine mitochondrial cytochrome bc1 complex, Science 281 (5373) (1998) 64–71, https://doi.org/10.1126/science.281.5373.64.
[5] P.H. Raven, Origin of eukaryotic cells, Evolution 25 (4) (1971) 737, https://doi.org/10.1111/j.1558-5646.1971.tb01930.x.
[6] R. Baradaran, J.M. Berrisford, G.S. Minhas, L.A. Sazanov, Crystal structure of the entire respiratory complex I, Nature 494 (7438) (2013) 443–448, https://doi.org/10.1038/nature11871.
[7] R.G. Efremov, R. Baradaran, L.A. Sazanov, The architecture of respiratory complex I, Nature 465 (7297) (2010) 441–445, https://doi.org/10.1038/nature09066.
[8] M.O. Ripple, N. Kim, R. Springett, Mammalian complex I pumps 4 protons per 2 electrons at high and physiological proton motive force in living cells, J. Biol. Chem. 288 (8) (2013) 5374–5380, https://doi.org/10.1074/jbc.M112.438945.
[9] L.A. Sazanov, A giant molecular proton pump: structure and mechanism of respiratory complex I, Nat. Rev. Mol. Cell Biol. 16 (6) (2015) 375–388, https://doi.org/10.1038/nrm3997.
[10] U. Khaniya, C. Gupta, X. Cai, J. Mao, D. Kaur, Y. Zhang, A. Singharoy, M. Gunner, Hydrogen bond network analysis reveals the pathway for the proton transfer in the E-channel of T. thermophilus Complex I, Biochimica et Biophysica Acta (BBA)-Bioenergetics 1861 (10) (2020) 148240, https://doi.org/10.1016/j.bbabio.2020.148240.
[11] J.M. Berrisford, R. Baradaran, L.A. Sazanov, Structure of bacterial respiratory complex I, Biochimica et Biophysica Acta (BBA)-Bioenergetics 1857 (7) (2016) 892–901, https://doi.org/10.1016/j.bbabio.2016.01.012.
[12] D. Kampjut, L.A. Sazanov, Structure of respiratory complex I–An emerging blueprint for the mechanism, Curr. Opin. Struct. Biol. 74 (2022) 102350, https://doi.org/10.1016/j.sbi.2022.102350.
[13] V.R. Kaila, Long-range proton-coupled electron transfer in biological energy conversion: towards mechanistic understanding of respiratory complex I, J. R. Soc. Interface 15 (141) (2018) 20170916, https://doi.org/10.1098/rsif.2017.0916.
[14] S.P. Balashov, Protonation reactions and their coupling in bacteriorhodopsin, Biochimica et Biophysica Acta (BBA)-Bioenergetics 1460 (1) (2000) 75–94, https://doi.org/10.1016/S0005-2728(00)00131-6.
[15] V.R. Kaila, M.I. Verkhovsky, M. Wikström, Proton-coupled electron transfer in cytochrome oxidase, Chem. Rev. 110 (12) (2010) 7062–7081, https://doi.org/10.1021/cr1002003.
[16] M. Wikström, Cytochrome c oxidase: 25 years of the elusive proton pump, Biochimica et Biophysica Acta (BBA)-Bioenergetics 1655 (2004) 241–247, https://doi.org/10.1016/j.bbabio.2003.07.013.
[17] M. Gunner, M. Amin, X. Zhu, J. Lu, Molecular mechanisms for generating transmembrane proton gradients, Biochimica et Biophysica Acta (BBA)-Bioenergetics 1827 (8–9) (2013) 892–913, https://doi.org/10.1016/j.bbabio.2013.03.001.
[18] M. Gunner, R. Koder, The design features cells use to build their transmembrane proton gradient, Phys. Biol. 14 (1) (2017) 013001, https://doi.org/10.1088/1478-3975/14/1/013001.
[19] V.R. Kaila, M. Wikström, G. Hummer, Electrostatics, hydration, and proton transfer dynamics in the membrane domain of respiratory complex I, Proc. Natl. Acad. Sci. 111 (19) (2014) 6988–6993, https://doi.org/10.1073/pnas.1319156111.
[20] V. Zickermann, C. Wirth, H. Nasiri, K. Siegmund, H. Schwalbe, C. Hunte, U. Brandt, Mechanistic insight from the crystal structure of mitochondrial complex I, Science 347 (6217) (2015) 44–49, https://doi.org/10.1126/science.1259859.
[21] X. Cai, C.Y. Son, J. Mao, D. Kaur, Y. Zhang, U. Khaniya, Q. Cui, M. Gunner, Identifying the proton loading site cluster in the ba3 cytochrome c oxidase that loads and traps protons, Biochimica et Biophysica Acta (BBA)-Bioenergetics 1861 (10) (2020) 148239, https://doi.org/10.1016/j.bbabio.2020.148239.
[22] D. Kaur, X. Cai, U. Khaniya, Y. Zhang, J. Mao, M. Mandal, M.R. Gunner, Tracing the pathways of waters and protons in photosystem II and cytochrome c oxidase, Inorganics 7 (2) (2019) 14, https://doi.org/10.3390/inorganics7020014.
[23] L. Yang, Å.A. Skjevik, W.-G.H. Du, L. Noodleman, R.C. Walker, A.W. Götz, Water exit pathways and proton pumping mechanism in B-type cytochrome c oxidase from molecular dynamics simulations, Biochimica et Biophysica Acta (BBA)-Bioenergetics 1857 (9) (2016) 1594–1606, https://doi.org/10.1016/j.bbabio.2016.06.005.
[24] P. Goyal, J. Lu, S. Yang, M. Gunner, Q. Cui, Changing hydration level in an internal cavity modulates the proton affinity of a key glutamate in cytochrome c oxidase, Proc. Natl. Acad. Sci. 110 (47) (2013) 18886–18891, https://doi.org/10.1073/pnas.1313908110.
[25] P. Wang, N. Dhananjayan, M.A. Hagras, A.A. Stuchebrukhov, Respiratory complex I: bottleneck at the entrance of quinone site requires conformational change for its opening, Biochimica et Biophysica Acta (BBA)-Bioenergetics 1862 (1) (2021) 148326, https://doi.org/10.1016/j.bbabio.2020.148326.
[26] I. Chung, D.N. Grba, J.J. Wright, J. Hirst, Making the leap from structure to mechanism: are the open states of mammalian complex I identified by cryoEM resting states or catalytic intermediates? Curr. Opin. Struct. Biol. 77 (2022) 102447 https://doi.org/10.1016/j.sbi.2022.102447.
[27] J. Hirst, Mitochondrial complex I, Annu. Rev. Biochem. 82 (2013) 551–575, https://doi.org/10.1146/annurev-biochem-070511-103700.
[28] C. Wirth, U. Brandt, C. Hunte, V. Zickermann, Structure and function of mitochondrial complex I, Biochimica et Biophysica Acta (BBA)-Bioenergetics 1857 (7) (2016) 902–914, https://doi.org/10.1016/j.bbabio.2016.02.013.
[29] A.-N.A. Agip, J.N. Blaza, J.G. Fedor, J. Hirst, Mammalian respiratory complex I through the lens of cryo-EM, Annu. Rev. Biophys. 48 (1) (2019) 165–184, https://doi.org/10.1146/annurev-biophys-052118-115704.
[30] N.A. Agip, J.N. Blaza, H.R. Bridges, C. Viscomi, S. Rawson, S.P. Muench, J. Hirst, Cryo-EM structures of complex I from mouse heart mitochondria in two biochemically defined states, Nat. Struct. Mol. Biol. 25 (7) (2018) 548–556, https://doi.org/10.1038/s41594-018-0073-1.
[31] A. Djurabekova, J. Lasham, O. Zdorevskyi, V. Zickermann, V. Sharma, Long-range electron proton coupling in respiratory complex I—insights from molecular simulations of the quinone chamber and antiporter-like subunits, Biochem. J. 481 (7) (2024) 499–514, https://doi.org/10.1042/BCJ20240009.
[32] E.G. Yoga, H. Angerer, K. Parey, V. Zickermann, Respiratory complex I–mechanistic insights and advances in structure determination, Biochimica et Biophysica Acta (BBA)-Bioenergetics 1861 (3) (2020) 148153, https://doi.org/10.1016/j.bbabio.2020.148153.
[33] H.R. Bridges, J.N. Blaza, Z. Yin, I. Chung, M.N. Pollak, J. Hirst, Structural basis of mammalian respiratory complex I inhibition by medicinal biguanides, Science 379 (6630) (2023) 351–357, https://doi.org/10.1126/science.ade3332.
[34] D.N. Grba, I. Chung, H.R. Bridges, A.-N.A. Agip, J. Hirst, Investigation of hydrated channels and proton pathways in a high-resolution cryo-EM structure of mammalian complex I, Science Advances 9 (31) (2023), https://doi.org/10.1126/sciadv.adi1359 p. eadi1359.
[35] D. Kampjut, L.A. Sazanov, The coupling mechanism of mammalian respiratory complex I, Science 370 (6516) (2020), https://doi.org/10.1126/science.abc4209 p. eabc4209.
[36] M. Narayanan, J.A. Sakyiama, M.M. Elguindy, E. Nakamaru-Ogiso, Roles of subunit NuoL in the proton pumping coupling mechanism of NADH: ubiquinone oxidoreductase (complex I) from Escherichia coli, The Journal of Biochemistry 160 (4) (2016) 205–215, https://doi.org/10.1093/jb/mvw027.
[37] J. Michel, J. DeLeon-Rangel, S. Zhu, K. Van Ree, S.B. Vik, Mutagenesis of the L, M, and N subunits of complex I from Escherichia coli indicates a common role in function, PloS One 6 (2) (2011) e17420, https://doi.org/10.1371/journal.pone.0017420.
[38] J. Torres-Bacete, E. Nakamaru-Ogiso, A. Matsuno-Yagi, T. Yagi, Characterization of the NuoM (ND4) subunit in Escherichia coli NDH-1: conserved charged residues essential for energy-coupled activities, J. Biol. Chem. 282 (51) (2007) 36914–36922, https://doi.org/10.1074/jbc.M707855200.
[39] M. Sato, P.K. Sinha, J. Torres-Bacete, A. Matsuno-Yagi, T. Yagi, Energy transducing roles of antiporter-like subunits in Escherichia coli NDH-1 with main focus on subunit NuoN (ND2), J. Biol. Chem. 288 (34) (2013) 24705–24716, https://doi.org/10.1074/jbc.M113.482968.
[40] M. Röpke, P. Saura, D. Riepl, M.C. Pöverlein, V.R. Kaila, Functional water wires catalyze long-range proton pumping in the mammalian respiratory complex I, J. Am. Chem. Soc. 142 (52) (2020) 21758–21766, https://doi.org/10.1021/jacs.0c09209.
[41] A. Di Luca, A.P. Gamiz-Hernandez, V.R. Kaila, Symmetry-related proton transfer pathways in respiratory complex I, Proc. Natl. Acad. Sci. 114 (31) (2017) E6314–E6321, https://doi.org/10.1073/pnas.1706278114.
[42] O. Haapanen, V. Sharma, Role of water and protein dynamics in proton pumping by respiratory complex I, Sci. Rep. 7 (1) (2017) 7747, https://doi.org/10.1038/s41598-017-07930-1.
[43] P. Tan, Z. Feng, L. Zhang, T. Hou, Y. Li, The mechanism of proton translocation in respiratory complex I from molecular dynamics, J. Recept. Signal Transduction 35 (2) (2015) 170–179, https://doi.org/10.3109/10799893.2014.942464.
[44] C. Mathiesen, C. Hägerhäll, Transmembrane topology of the NuoL, M and N subunits of NADH: quinone oxidoreductase and their homologues among membrane-bound hydrogenases and bona fide antiporters, Biochimica et Biophysica Acta (BBA)-Bioenergetics 1556 (2–3) (2002) 121–132, https://doi.org/10.1016/S0005-2728(02)00343-2.
[45] J. Zhuang, J.H. Amoroso, R. Kinloch, J.H. Dawson, M.J. Baldwin, B.R. Gibney, Evaluation of electron-withdrawing group effects on heme binding in designed proteins: implications for heme a in cytochrome c oxidase, Inorg. Chem. 45 (2006) 4685–4694, https://doi.org/10.1021/ic060072c.
[46] J.C. Fontecilla-Camps, A. Volbeda, C. Cavazza, Y. Nicolet, Structure/function relationships of [NiFe]-and [FeFe]-hydrogenases, Chem. Rev. 107 (10) (2007) 4273–4303, https://doi.org/10.1021/cr050195z.
[47] R.G. Efremov, L.A. Sazanov, The coupling mechanism of respiratory complex I—a structural and evolutionary perspective, Biochimica et Biophysica Acta (BBA)-Bioenergetics 1817 (10) (2012) 1785–1795, https://doi.org/10.1016/j.bbabio.2012.02.015.
[48] V.R. Kaila, Resolving chemical dynamics in biological energy conversion: long-range proton-coupled electron transfer in respiratory complex I, Acc. Chem. Res. 54 (24) (2021) 4462–4473, https://doi.org/10.1021/acs.accounts.1c00524.
[49] L.A. Sazanov, The mechanism of coupling between electron transfer and proton translocation in respiratory complex I, J. Bioenerg. Biomembr. 46 (2014) 247–253, https://doi.org/10.1007/s10863-014-9554-z.
[50] M. Verkhovskaya, D.A. Bloch, Energy-converting respiratory complex I: on the way to the molecular mechanism of the proton pump, Int. J. Biochem. Cell Biol. 45 (2) (2013) 491–511, https://doi.org/10.1016/j.biocel.2012.08.024.
[51] C. Gupta, U. Khaniya, C.K. Chan, F. Dehez, M. Shekhar, M. Gunner, L. Sazanov, C. Chipot, A. Singharoy, Charge transfer and chemo-mechanical coupling in respiratory complex I, J. Am. Chem. Soc. 142 (20) (2020) 9220–9230, https://doi.org/10.1021/jacs.9b13450.
[52] J. Gutiérrez-Fernández, K. Kaszuba, G.S. Minhas, R. Baradaran, M. Tambalo, D. T. Gallagher, L.A. Sazanov, Key role of quinone in the mechanism of respiratory

complex I, Nat. Commun. 11 (1) (2020) 4135, https://doi.org/10.1038/s41467-020-17957-0.
[53] C. Gupta, U. Khaniya, C.K. Chan, M. Gunner, C. Chipot, F. Dehez, A. Singharoy, Chemomechanical coupling of mitochondrial complex I, Biophys. J. 116 (3) (2019) 155a, https://doi.org/10.1016/j.bpj.2018.11.858.
[54] V. Sharma, G. Belevich, A.P. Gamiz-Hernandez, T. Róg, I. Vattulainen, M. L. Verkhovskaya, M. Wikström, G. Hummer, V.R. Kaila, Redox-induced activation of the proton pump in the respiratory complex I, Proc. Natl. Acad. Sci. 112 (37) (2015) 11571–11576, https://doi.org/10.1073/pnas.150376111.
[55] R.J. Wei, Y. Zhang, J. Mao, D. Kaur, U. Khaniya, M. Gunner, Comparison of proton transfer paths to the QA and QB sites of the Rb. Sphaeroides photosynthetic reaction centers, Photosynth. Res. 152 (2) (2022) 153–165, https://doi.org/10.1007/s11120-022-00906-x.
[56] U. Khaniya, J. Mao, R.J. Wei, M. Gunner, Characterizing protein protonation microstates using Monte Carlo sampling, J. Phys. Chem. B. 126 (13) (2022) 2476–2485, https://doi.org/10.1021/acs.jpcb.2c00139.
[57] Y. Song, J. Mao, M.R. Gunner, MCCE2: improving protein pKa calculations with extensive side chain rotamer sampling, J. Comput. Chem. 30 (14) (2009) 2231–2247, https://doi.org/10.1002/jcc.21222.
[58] C.H. Chang, K. Kim, Density functional theory calculation of bonding and charge parameters for molecular dynamics studies on [FeFe] hydrogenases, J. Chem. Theory Comput. 5 (4) (2009) 1137–1145, https://doi.org/10.1021/ct800342w.
[59] M.L. Verkhovskaya, N. Belevich, L. Euro, M. Wikström, M.I. Verkhovsky, Real-time electron transfer in respiratory complex I, Proc. Natl. Acad. Sci. 105 (10) (2008) 3763–3767, https://doi.org/10.1073/pnas.0711249105.
[60] H.R. Bridges, E. Bill, J. Hirst, Mossbauer spectroscopy on respiratory complex I: the iron–sulfur cluster ensemble in the NADH-reduced enzyme is partially oxidized, Biochemistry 51 (1) (2012) 149–158, https://doi.org/10.1021/bi201644x.
[61] M.M. Roessler, M.S. King, A.J. Robinson, F.A. Armstrong, J. Harmer, J. Hirst, Direct assignment of EPR spectra to structurally defined iron-sulfur clusters in complex I by double electron–electron resonance, Proc. Natl. Acad. Sci. 107 (5) (2010) 1930–1935, https://doi.org/10.1073/pnas.0908050107.
[62] P.L. Freddolino, K.H. Gardner, K. Schulten, Signaling mechanisms of LOV domains: new insights from molecular dynamics studies, Photochem. Photobiol. Sci. 12 (7) (2013) 1158–1170, https://doi.org/10.1039/c3pp25400c.
[63] R.J. Gowers, M. Linke, J. Barnoud, T.J.E. Reddy, M.N. Melo, S.L. Seyler, J. Domanski, D.L. Dotson, S. Buchoux, I.M. Kenney, MDAnalysis: A Python Package for The Rapid Analysis of Molecular Dynamics Simulations, Los Alamos National Laboratory (LANL), Los Alamos, NM (United States), 2019, https://doi.org/10.25080/Majora-629e541a-00e.
[64] N. Michaud-Agrawal, E.J. Denning, T.B. Woolf, O. Beckstein, MDAnalysis: a toolkit for the analysis of molecular dynamics simulations, J. Comput. Chem. 32 (10) (2011) 2319–2327, https://doi.org/10.1002/jcc.21787.
[65] T. Tubiana, J.-C. Carvaillo, Y. Boulard, S. Bressanelli, TTClust: a versatile molecular simulation trajectory clustering program with graphical summaries, J. Chem. Inf. Model. 58 (11) (2018) 2178–2182, https://doi.org/10.1021/acs.jcim.8b00512.
[66] Y. Song, J. Mao, M.R. Gunner, Calculation of proton transfers in bacteriorhodopsin bR and M intermediates, Biochemistry 42 (33) (2003) 9875–9888, https://doi.org/10.1021/bi034482d.
[67] M. Gunner, X. Zhu, M.C. Klein, MCCE analysis of the pKas of introduced buried acids and bases in staphylococcal nuclease, Proteins: Struct., Funct., Bioinf. 79 (12) (2011) 3306–3319, https://doi.org/10.1002/prot.23124.
[68] X. Cai, K. Haider, J. Lu, S. Radic, C.Y. Son, Q. Cui, M. Gunner, Network analysis of a proposed exit pathway for protons to the P-side of cytochrome c oxidase, Biochimica et Biophysica Acta (BBA)-Bioenergetics 1859 (10) (2018) 997–1005, https://doi.org/10.1016/j.bbabio.2018.05.010.
[69] M.E. Mühlbauer, P. Saura, F. Nuber, A. Di Luca, T. Friedrich, V.R. Kaila, Water-gated proton transfer dynamics in respiratory complex I, J. Am. Chem. Soc. 142 (32) (2020) 13718–13728, https://doi.org/10.1021/jacs.0c02789.
[70] M.A. Tocilescu, U. Fendel, K. Zwicker, S. Dröse, S. Kerscher, U. Brandt, The role of a conserved tyrosine in the 49-kDa subunit of complex I for ubiquinone binding and reduction, Biochimica et Biophysica Acta (BBA)-Bioenergetics 1797 (6–7) (2010) 625–632, https://doi.org/10.1016/j.bbabio.2010.01.029.
[71] M.A. Tocilescu, U. Fendel, K. Zwicker, S. Kerscher, U. Brandt, Exploring the ubiquinone binding cavity of respiratory complex I, J. Biol. Chem. 282 (40) (2007) 29514–29520, https://doi.org/10.1074/jbc.M704519200.
[72] A.P. Gamiz-Hernandez, A. Jussupow, M.P. Johansson, V.R. Kaila, Terminal electron–proton transfer dynamics in the quinone reduction of respiratory complex I, J. Am. Chem. Soc. 139 (45) (2017) 16282–16288, https://doi.org/10.1021/jacs.7b08486.
[73] L.A. Sazanov, Respiratory complex I: mechanistic and structural insights provided by the crystal structure of the hydrophilic domain, Biochemistry 46 (9) (2007) 2275–2288, https://doi.org/10.1021/bi602508x.
[74] R.G. Efremov, L.A. Sazanov, Structure of the membrane domain of respiratory complex I, Nature 476 (7361) (2011) 414–420, https://doi.org/10.1038/nature10330.
[75] P.K. Sinha, J. Torres-Bacete, E. Nakamaru-Ogiso, N. Castro-Guerrero, A. Matsuno-Yagi, T. Yagi, Critical roles of subunit NuoH (ND1) in the assembly of peripheral subunits with the membrane domain of Escherichia coli NDH-1, J. Biol. Chem. 284 (15) (2009) 9814–9823, https://doi.org/10.1074/jbc.M809468200.
[76] J. Lu, M. Gunner, Characterizing the proton loading site in cytochrome c oxidase, Proc. Natl. Acad. Sci. 111 (34) (2014) 12414–12419, https://doi.org/10.1073/pnas.1407187111.
[77] J.A. Letts, K. Fiedorczuk, G. Degliesposti, M. Skehel, L.A. Sazanov, Structures of respiratory supercomplex I+ III2 reveal functional and conformational crosstalk, Mol. Cell 75 (6) (2019) 1131–1146, e6, https://doi.org/10.1016/j.molcel.2019.07.022.
[78] S. Steimle, M. Willistein, P. Hegger, M. Janoschke, H. Erhardt, T. Friedrich, Asp563 of the horizontal helix of subunit NuoL is involved in proton translocation by the respiratory complex I, FEBS Lett. 586 (6) (2012) 699–704, https://doi.org/10.1016/j.febslet.2012.01.056.
[79] L. Euro, G. Belevich, M.I. Verkhovsky, M. Wikström, M. Verkhovskaya, Conserved lysine residues of the membrane subunit NuoM are involved in energy conversion by the proton-pumping NADH: ubiquinone oxidoreductase (Complex I), Biochimica et Biophysica Acta (BBA)-Bioenergetics 1777 (9) (2008) 1166–1172, https://doi.org/10.1016/j.bbabio.2008.06.001.
[80] J. Torres-Bacete, P.K. Sinha, A. Matsuno-Yagi, T. Yagi, Structural contribution of C-terminal segments of NuoL (ND5) and NuoM (ND4) subunits of complex I from Escherichia coli, J. Biol. Chem. 286 (39) (2011) 34007–34014, https://doi.org/10.1074/jbc.M111.260968.
[81] M.-C. Kao, S. Di Bernardo, M. Perego, E. Nakamaru-Ogiso, A. Matsuno-Yagi, T. Yagi, Functional roles of four conserved charged residues in the membrane domain subunit NuoA of the proton-translocating NADH-quinone oxidoreductase from Escherichia coli, J. Biol. Chem. 279 (31) (2004) 32360–32366, https://doi.org/10.1074/jbc.M403885200.
[82] S. Kurki, V. Zickermann, M. Kervinen, I. Hassinen, M. Finel, Mutagenesis of three conserved Glu residues in a bacterial homologue of the ND1 subunit of complex I affects ubiquinone reduction kinetics but not inhibition by dicyclohexylcarbodiimide, Biochemistry 39 (44) (2000) 13496–13502, https://doi.org/10.1021/bi001134s.
[83] G. Belevich, L. Euro, M. Wikström, M. Verkhovskaya, Role of the conserved arginine 274 and histidine 224 and 228 residues in the NuoCD subunit of complex I from Escherichia coli, Biochemistry 46 (2) (2007) 526–533, https://doi.org/10.1021/bi062062t.
[84] G.E. Crooks, G. Hon, J.-M. Chandonia, S.E. Brenner, WebLogo: a sequence logo generator, Genome Res. 14 (6) (2004) 1188–1190, http://www.genome.org/cgi/doi/10.1101/gr.849004.
[85] J. Gu, T. Liu, R. Guo, L. Zhang, M. Yang, The coupling mechanism of mammalian mitochondrial complex I, Nat. Struct. Mol. Biol. 29 (2) (2022) 172–182, https://doi.org/10.1038/s41594-022-00722-w.
[86] A.A. Stuchebrukhov, T. Hayashi, Single protonation of the reduced quinone in respiratory complex I drives four-proton pumping, FEBS Lett. 597 (2) (2023) 237–245, https://doi.org/10.1002/1873-3468.14518.
[87] L.A. Sazanov, From the 'black box'to 'domino effect'mechanism: what have we learned from the structures of respiratory complex I, Biochem. J. 480 (5) (2023) 319–333, https://doi.org/10.1042/BCJ20210285.
[88] O. Zdorevskyi, A. Djurabekova, J. Lasham, V. Sharma, Horizontal proton transfer across the antiporter-like subunits in mitochondrial respiratory complex I, Chem. Sci. 14 (23) (2023) 6309–6318, https://doi.org/10.1039/D3SC01427D.
[89] V. Kravchuk, O. Petrova, D. Kampjut, A. Wojciechowska-Bason, Z. Breese, L. Sazanov, A universal coupling mechanism of respiratory complex I, Nature 609 (7928) (2022) 808–814, https://doi.org/10.1038/s41586-022-05199-7.
[90] Sazanov, L.A. and P. Hinchliffe, Structure of the hydrophilic domain of respiratory complex I from Thermus thermophilus. science, 2006. 311(5766): p. 1430–1436, doi:https://doi.org/10.1126/science.1123809.